scientific reports

OPEN

Friction stir welding of Haynes 282 Ni superalloy by using a novel hemispherical tool

Abhishek Sharma[1✉], Takuya Miura[1], Yoshiaki Morisada[1], Kohsaku Ushioda[1], Sukhdeep Singh[2] & Hidetoshi Fujii[1✉]

In the present investigation, friction stir welding (FSW) of a gamma prime (γ′) strengthened Haynes 282 nickel-base superalloy by using a novel hemispherical tool is documented. A joint efficiency of ~ 96% was achieved in the as-welded condition, which further increased to ~ 100% after two-step post-weld aging heat treatment. An extremely fine (~ 2 µm) grained microstructure was observed in the FSWed region compared with the coarse (~ 48 µm) grain base metal region. The carbides (MC and $M_{23}C_6$) and γ′ precipitates are identified as the important microstructural constituent phases observed in the welded region. The aging heat treatment resulted in the precipitation of the γ′ strengthening phase and altered the morphology of the $M_{23}C_6$ carbide phase in the welded region from a continuous film to discrete particles at the grain boundaries. The preliminary results concerning tool life suggest that no significant tool wear occurs at least up to a welding distance of 200 mm. Therefore, the novel hemispherical tool design allows the successful FSW of high-temperature application materials without any significant tool wear or high heat generation.

Keywords Friction stir welding (FSW), Hemispherical tool, Haynes 282, Precipitation strengthening, Ni-based superalloy

Haynes 282 (H282) is a γ′ strengthened nickel-base superalloy with high-temperature applications in the turbine components (both gas and steam) of jet engines and advanced ultra supercritical thermal power plants. The H282 alloy is known for its excellent creep resistance and high-temperature tensile strength at an operating temperature of up to 760 °C[1]. The H282 alloy also exhibited good weldability owing to the low volume fraction of the γ′ phase (~ 19%) in the alloy[2]. However, during fusion welding of H282 alloys, the weld zone microstructure is significantly affected by micro segregation and nonequilibrium phase transformations during solidification[3,4]. The interdendritic micro segregation also leads to the nucleation of intermetallic secondary solidification constituents along the dendrite interstices as well as the inhomogeneous distribution of second-phase precipitates[5]. Most commonly, the strengthening grain boundary carbides (MC, $M_{23}C_6$) segregate in the interdendritic regions and deteriorate the high-temperature performance of the joint[6]. Numerous previous studies confirmed the presence of this grain boundary liquation and cracking in the heat-affected zone (HAZ) of the fusion welded H282 alloy[7,8].

Friction stir welding (FSW) is a solid-state joining technique that is industrially accepted for soft metallic materials such as aluminum alloys[9,10]. The FSW has the potential to overcome the shortcomings of fusion welding of H282 alloys owing to the low heat input and absence of interdendritic second-phase segregation. However, the FSW of high-temperature strength materials requires an efficient tool material and design to withstand high processing temperatures and forces. Moreover, the FSW tool probe is the most delicate part and is often subjected to tool wear and potential fracture during the FSW of high-temperature materials. The FSW of solid-solution strengthened Ni base alloys such as Inconel 600[11], Inconel 625[12], and Inconel 718[13] has already been reported by several researchers. However, the FSW of γ′ strengthened alloys (such as H282 alloys) is very limited. The primary reason for this scarcity is FSW tool wear during the welding of these alloys. Komarasamy et al.[14] conducted the first and only available study on the FSW of H282 alloy to date. In their study, FSW was made possible on H282 alloy by using a polycrystalline boron nitride (PCBN) tool with argon shielding to avoid oxidation and water cooling to avoid machine spindle overheating. The authors also conducted welding at a very low rotational speed of 60–80 RPM at a welding speed of 25 mm/min. The use of the PCBN tool, argon shielding, water cooling, and low rotational speed demonstrate the difficulties associated with the FSW of H282 alloy.

[1]Joining & Welding Research Institute, Osaka University, Osaka 567-0047, Japan. [2]Department of Engineering Science, University West, Trollhättan SE-46186, Sweden. ✉email: sharma.abhishek.jwri@osaka-u.ac.jp; fujii.hidetoshi.jwri@osaka-u.ac.jp

Ni	Cr	Co	Mo	Ti	Al	Mn	Fe	Si	C	B
Bal.	19.49	10.36	8.55	2.16	1.52	0.05	0.37	0.05	0.072	0.05

Table 1. Chemical composition of the as-received wrought H282 alloy.
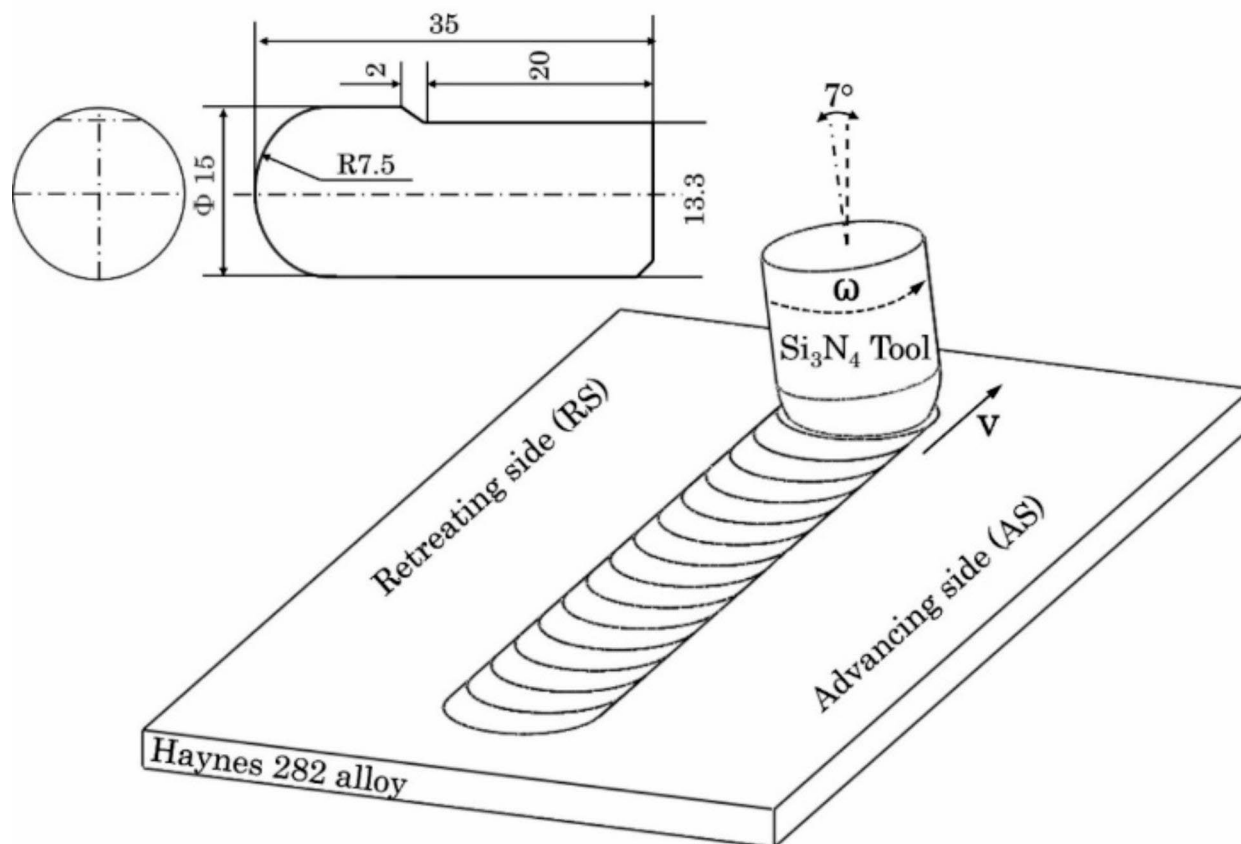
Fig. 1. Schematic representation of FSW with a hemispherical tool and hemispherical tool design. (All dimensions are in mm).

The newly designed hemispherical tool (HT) tilted towards retreating side (RS) offers a practical solution to the above-mentioned issues encountered with the FSW of H282 alloy[15]. This innovative HT design features a dome that functions as both the shoulder and the probe. The hemispherical shape reduces frictional heat generation and improve the tool life without affecting the weld strength[16]. Additionally, the design eliminates the risk of probe fracture, which is a frequent challenge when high-temperature strength materials are welded. Therefore, in the present study, a novel hemispherical tool made of silicon nitride (Si_3N_4) is proposed for the efficient FSW of H282 alloy. Here, Si_3N_4 is chosen as the tool material due to its excellent fracture toughness at high temperatures[17]. Additionally, Si_3N_4 remains stable at elevated welding temperatures and is more cost-effective than PCBN tools[18]. The joint efficiency was evaluated under the as-welded condition and after two-stage post-weld heat treatment (aging). The results are corroborated by various advanced material characterization techniques, such as Scanning Electron Microscope (SEM), Electron Backscattered Diffraction (EBSD), Transmission Electron Microscope (TEM), Digital Image Correlation (DIC), etc.

Materials and methods
Materials
Soft annealed Haynes 282 Ni superalloy (H282) plates with dimensions of 50 mm (w) × 75 mm (l) × 3.2 mm (t) were purchased from Haynes International. The chemical composition of the base material is presented in Table 1.

Material processing
FSW was conducted on H282 plates via a "bead-on-plate" scheme. The tool used for the FSW was made of silicon nitride (Si_3N_4) and has a dimension of 15 mm diameter. The tool geometry is depicted in Fig. 1. The FSW was

conducted in a position-controlled setting with a tool rotational speed of 400 RPM, welding speed of 30 mm/min, plunge depth of 2.5 mm, and tool tilt angle of 7° toward the retreating side (RS). The tilt angle of 7° toward the RS was selected based on our previously published study on the hemispherical tool design concept[19]. The axial load during FSW was measured by using a load cell built into the FSW setup. The temperature at the weld zone was measured by using a thermal imaging camera with an emissivity of 0.54. Following welding, the two-stage aging treatment was conducted on the FSWed joints as recommended by Haynes International. The two stages involved in the aging treatment were as follows: (i) heating at 1010 °C for 2 h followed by air cooling and (ii) heating at 788 °C for 8 h followed by air cooling.

Microstructural characterization

The specimens for microstructural characterization were obtained perpendicular to the welding direction using wire electrical discharge machining (EDM; Sodick, AG360L). For microstructural analysis, the specimens were prepared following standard metallographic procedures, which involved progressive grinding with abrasive paper up to 4000 grit, followed by polishing on a cloth with a 1 μm diamond suspension. Subsequently, the specimens were electropolished in a solution of ethanol and perchloric acid, maintained at -10 °C, with a voltage of 20 V for 8 s. The microstructural characterization of the specimens was performed via a field emission scanning electron microscope (SEM, JSM-7001FA) equipped with EBSD and energy dispersive spectroscopy (EDS). The working distance (WD), voltage and step size for the SEM and EBSD measurements were 15 mm, 15 kV and 30 nm, respectively. Transmission electron microscopy (TEM, JEM-2100 F) was used to identify the γ′ precipitates and carbide phases in the as welded and aged specimens. The thin foil specimens for TEM were prepared by using a focused ion-beam system (FIB; HITACHI FB-2000 A).

Mechanical testing

The transverse tensile test specimen of dimensions 12 mm gauge length and 3 mm width were obtained by using a EDM. The thickness of the tensile specimens was reduced from 3.2 mm (as-received material thickness) to 2.5 mm (plunge depth) by using a abrasive paper grinding. Room-temperature tensile testing was conducted on an Instron universal testing machine at a strain rate of 1×10^{-3} s^{-1}. The strain measurement and localized strain mapping were carried out via DIC following the methods of our previous study[20]. The microhardness was evaluated at the center of the weld zone (along the thickness) by using a microhardness tester (Future Tech, FM-800) at a load of 100 kgf and a dwell time of 15 s. Figure 1s (supplementary information) illustrates the scheme for the tensile specimen and microhardness measurement.

Results and discussion
Microstructural evolution

Figure 2(a)–(c) shows the temperature profile and axial load measurement during the FSW of H282 alloy. The temperature and axial load profiles demonstrate a uniform axial load (~ 12 kN) and a constant temperature of ~ 1050 °C during the entire welding run. Interestingly, the maximum temperature was always observed on the advancing side (AS) of the weld zone, as shown in Fig. 2(a). As explained in our previous study, this phenomenon is attributed to the presence of a continuous contact zone on the AS as compared with the intermittent contact zone on the RS[19]. Therefore, although the local material flow velocities are greater on the RS, the intermittent contact between consecutive material layers results in a lower temperature on the RS. The detailed mechanism is discussed later in this paper. Figure 2 (d) shows the weld seam profile obtained with the set of tool tilt angles and plunge depth. Notably, the cross-sectional thinning observed in the AS aligns with our previous study[19]. This thinning is primarily attributed to the tilting of the tool on the RS. The tilt angle leads to the asymmetric contact of the tool with the substrate material and because of it a complex material flow is generated. This complex material flow associated with the HT is influenced primarily by the combination of the limiting constraining angle and the linear tool velocity. However, a detailed discussion of the factors affecting AS thinning is beyond the scope of the present research and can be found in our previous study[19].

Figure 3 (a-b) & (c-d) shows backscattered electron (BS-SEM) micrographs of the as-received wrought H282 alloy under soft annealing conditions and after two-step aging treatment, respectively. The microstructure of the soft-annealed alloy consists of a coarse-grained structure with primary MC (Ti- and Mo-rich) and secondary $M_{23}C_6$ (Cr-rich) carbides, indicated as 1 and 2 in Fig. 3 (a), respectively. These primary and secondary phase carbides are identified based on the EDS analysis presented in Table 2. Moreover, the γ′ precipitates could not be observed via SEM, and the grain boundaries were mainly free from carbides. The solution annealing temperature of H282 alloy is usually accompanied by the dissolution of $M_{23}C_6$ grain boundary (GB) carbides. Therefore, these GB carbides appear occasionally and are isolated in the matrix material. The microstructure after direct aging treatment shows no grain growth of the base material. The MC and $M_{23}C_6$ carbides can be observed in the microstructure, as shown in Fig. 3(c). Notably, discrete $M_{23}C_6$ carbides can be observed preferentially decorating the grain boundaries (see Fig. 3(d)). The first step of the aging treatment (1010 °C/2 h) leads to the nucleation of these discrete GB carbides, followed by their stabilization and nucleation of γ′ precipitates in the second stage of aging. The EDS analysis (Table 2) confirmed that these grain boundary precipitates were Cr-rich $M_{23}C_6$ carbide phases.

Figure 4 shows the microstructural changes across different zones of the FSWed H282 alloy. Figure 4 (a) presents a low-magnification BS-SEM image of the joint, highlighting a well-defined weld zone with a clear contrast between the fine-grained stir zone and the coarse-grained base material region. Figure 4(b) and (d) display high-magnification micrographs of the stir zone (SZ)/thermo-mechanically affected zone (TMAZ) interface on the advancing side (AS) and retreating side (RS), respectively. Both AS and RS exhibit a narrow TMAZ, but no distinct HAZ is visible on either side of the weld zone. This absence of a noticeable HAZ is mainly due to the inherent thermal stability of the H282 alloy at high temperatures. Additionally, the heat input during
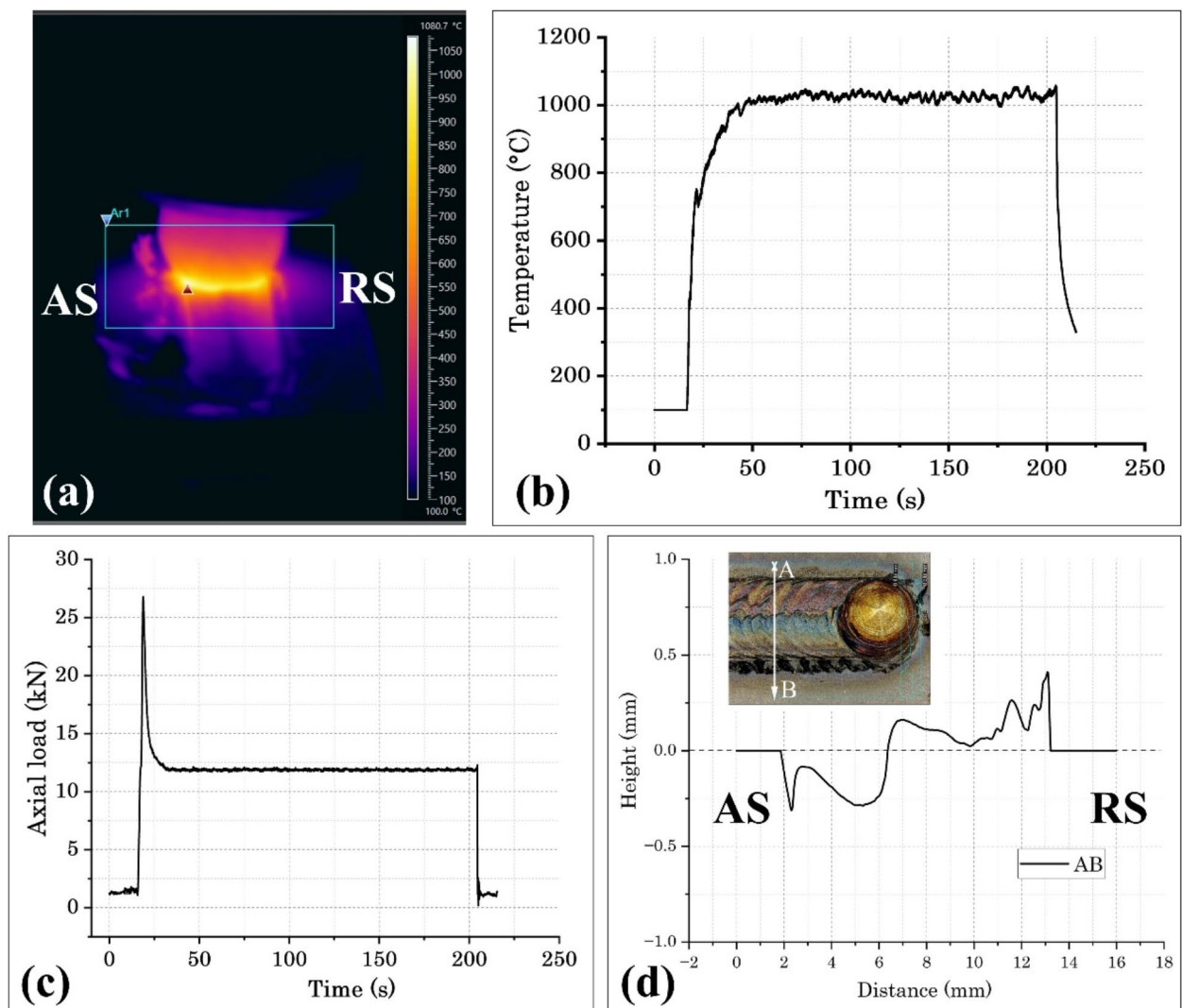
Fig. 2. (a) Thermal image, (b)maximum temperature profile, (c) axial load profile, and (d) weld profile of the joint.

FSW with a hemispherical tool is less intense than that during fusion welding techniques, where a more clearly defined HAZ is typically observed[21]. The high-magnification micrograph of the SZ (see Fig. 4(c)) depicts a fine-grained microstructure with dispersed carbide phases.

Figure 4 (e-g) and (h-j) present the EBSD inverse pole figure (IPF) maps of the base material and FSW joints in the as-welded and aged conditions, respectively. The EBSD measurements were conducted at two locations along the thickness of the SZ, as represented by X and Y in Fig. 4(a). The base metal (BM) microstructure (Fig. 4(e)) under soft-annealed conditions has a coarse grain size of ~ 48 µm, which remains almost unchanged to ~ 45 µm after aging heat treatment (Fig. 4(h)). Irrespective of the heat treatment, the base metal microstructure consists of annealing twins, which is consistent with previous investigations on H282 alloy[22].

The microstructure of the SZ demonstrated that a dynamically recrystallized fine grain structure formed as a result of high-temperature severe plastic deformation of the alloy. However, a through-thickness microstructural inhomogeneity can be visualized with the equiaxed fine-grained (~ 2 µm) microstructure at the top region and a relatively coarse-grained (~ 7 µm) microstructure at the bottom region, as depicted in Fig. 4 (f) and (g), respectively. This observation contradicts the previous study on FSW of H282 alloy conducted by Komarasamy et al.[14] and is attributed to the difference in the material flow mechanics associated with the hemispherical tool profile. Komarasamy et al.[14] used a conventional FSW tool where the maximum heat is generated at the top section because of shoulder/substrate frictional interactions. However, in the hemispherical profiled tool, the material flow mechanics are complex and are discussed here as follows. Figure 5 shows a schematic representation of the temperature gradient across the thickness of the weld zone obtained by the hemispherical-shaped tool profile tilted towards RS. In Zone A, the frictional interaction between the parent material and tool is continuous. The temperature decreases along the thickness due to the reduced dome radius per the tool profile. However, in Zone B, although the local velocities are higher (due to higher radii), the occurrence of intermittent
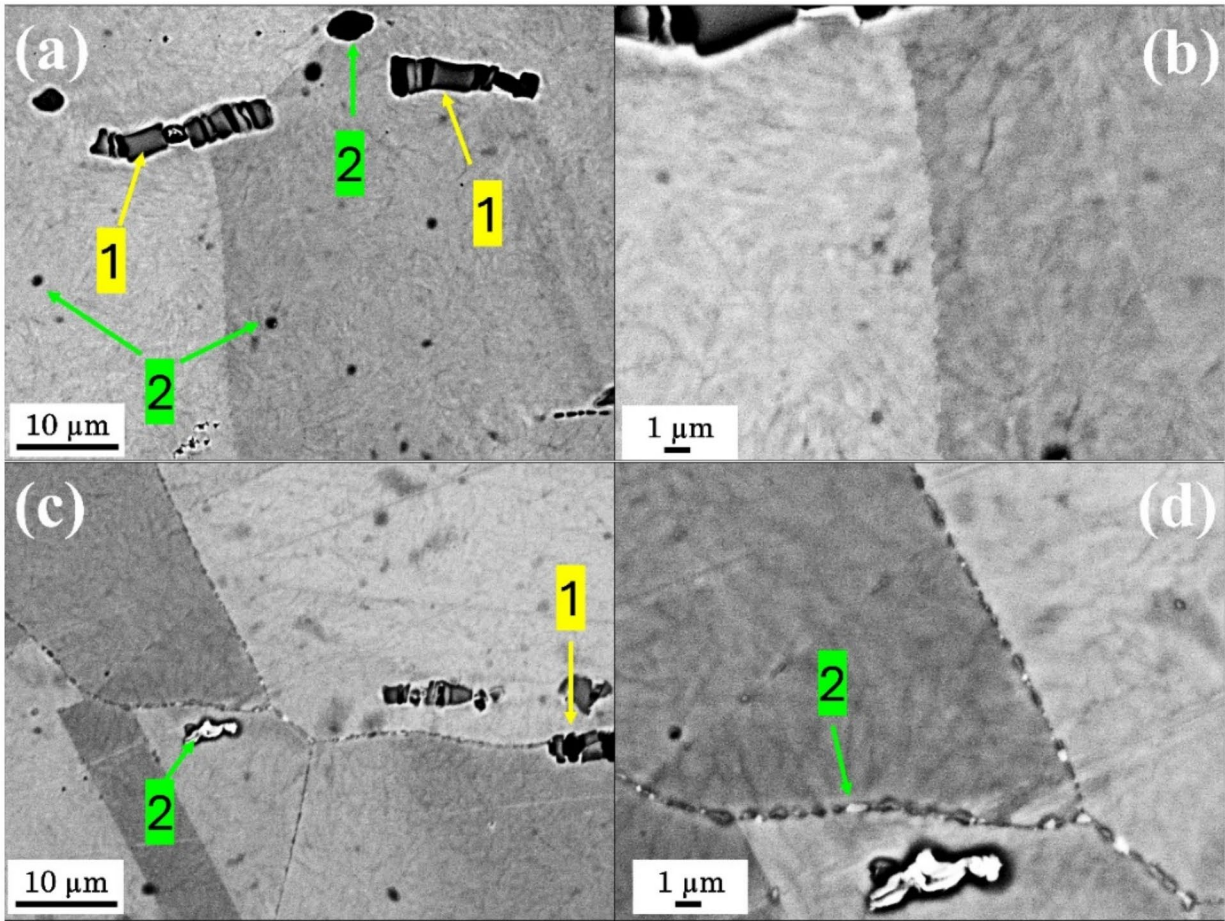
Fig. 3. BS-SEM micrographs of the (a-b) as-received wrought H282 alloy and (c-d) after two-step aging treatment.

Analysis point	Ni	Mo	Cr	Ti	Al
As received					
Ti-Mo rich phase (MC): **1**	18.50	30.29	9.29	39.74	0.53
Cr-rich phase ($M_{23}C_6$): **2**	63.06	8.92	23.73	2.21	1.59
Aged					
Ti-Mo rich phase (MC): **1**	2.64	36.48	2.77	56.06	-
Cr-rich phase ($M_{23}C_6$): **2**	64.85	8.56	22.86	2.48	1.25

Table 2. EDS elemental composition (at%) of the points shown in Fig. 3.

contact results in a lower temperature than the maximum radius of Zone A[19]. The EBSD measurement at X (Fig. 4(f) and (i)) falls under Zone B and therefore the fine grain size is justified in the top region compared with the bottom region (Y). Interestingly, irrespective of the EBSD measurement location, the grain size of the SZ is unaffected by the aging treatment owing to the grain boundary stabilization by the $M_{23}C_6$ carbide phases that precipitated during the first step of the two-stage aging heat treatment.

Figure 6 shows BS-SEM micrographs of the SZ of FSWed joints before and after aging heat treatment. The EDS elemental composition detailed in Table 3 verifies that the carbide phases (MC and $M_{23}C_6$) present in the FSWed specimens are consistent with those found in the wrought alloy. However, there is a notable difference in the morphology of the $M_{23}C_6$ secondary precipitates between the as-welded and aged specimens, as illustrated in Fig. 6(b) and (d). In the as-welded state, the $M_{23}C_6$ carbide phase exhibited a nearly continuous film and ledges protruding into the matrix, whereas after aging, the $M_{23}C_6$ phases displayed a discrete morphology. The continuous film-type carbide morphology indicates a prevalence (analogy) of low-temperature (< 750 °C) annealing conditions as a result of post-weld cooling[4]. This continuous film-type carbide morphology is usually detrimental to the ductility and toughness of the material. On the other hand, the discrete $M_{23}C_6$ phase that
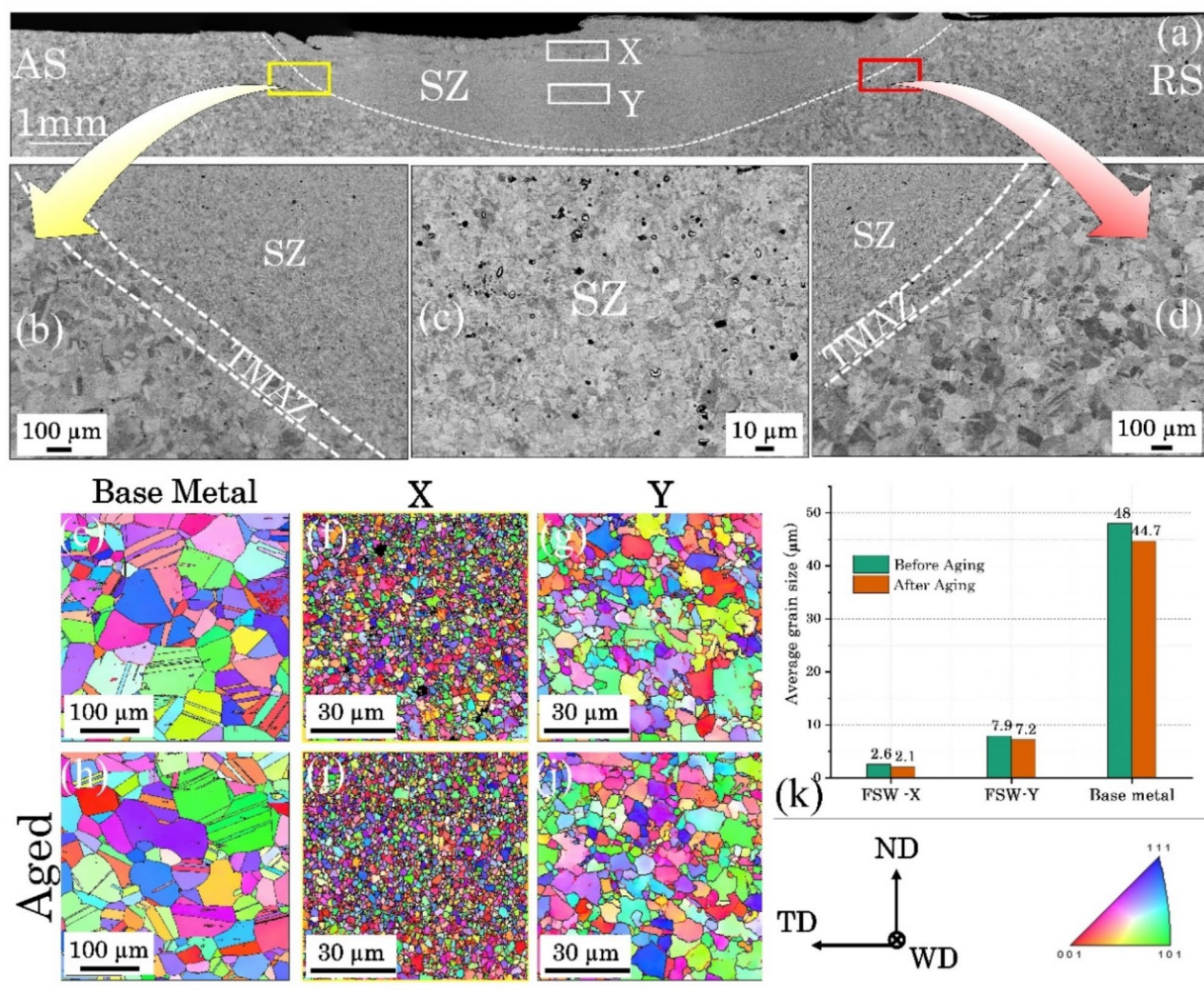
Fig. 4. BS-SEM micrographs of the (a) weld zone, (b) SZ/TMAZ interface on the AS, (c) SZ, and (d) SZ/TMAZ interface on the RS. EBSD IPF maps of the base metal (BM) (e) before aging and (h) after aging. EBSD IPF maps of the FSWed alloy (f-g) before aging, (i-j) after aging, and (k) average grain size at various locations.
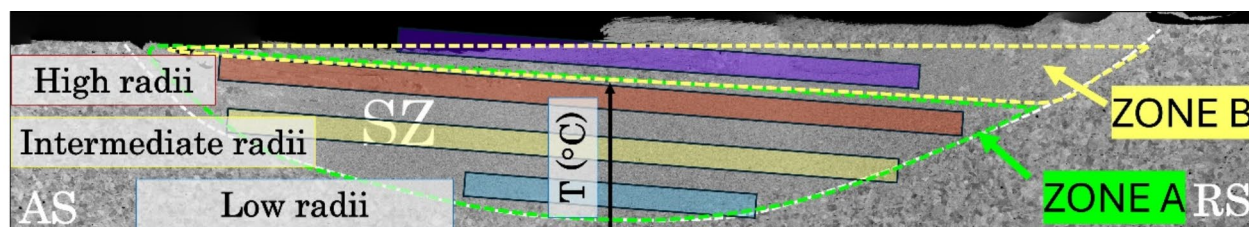

Fig. 5. Schematic representation of the thermal gradient in the weld zone formed during FSW with a hemispherical tool.

precipitated at the grain boundaries in the aged specimen represents a characteristic feature of the two-step aging treatment associated with the H282 alloy.

The BS-SEM micrograph of the aged specimen (Fig. 6(d)) indicates precipitation of the $M_{23}C_6$ phase predominantly at the grain boundaries. The $M_{23}C_6$ phase has a low driving force for precipitation, which makes it more likely to form in kinetically favourable locations such as grain boundaries. These grain boundaries lower the energy barrier for precipitation, making them preferential sites for this process. However, in the study conducted by Komaraswamy et al.[14], the authors reported the dominant intragranular dispersion of the Cr-rich
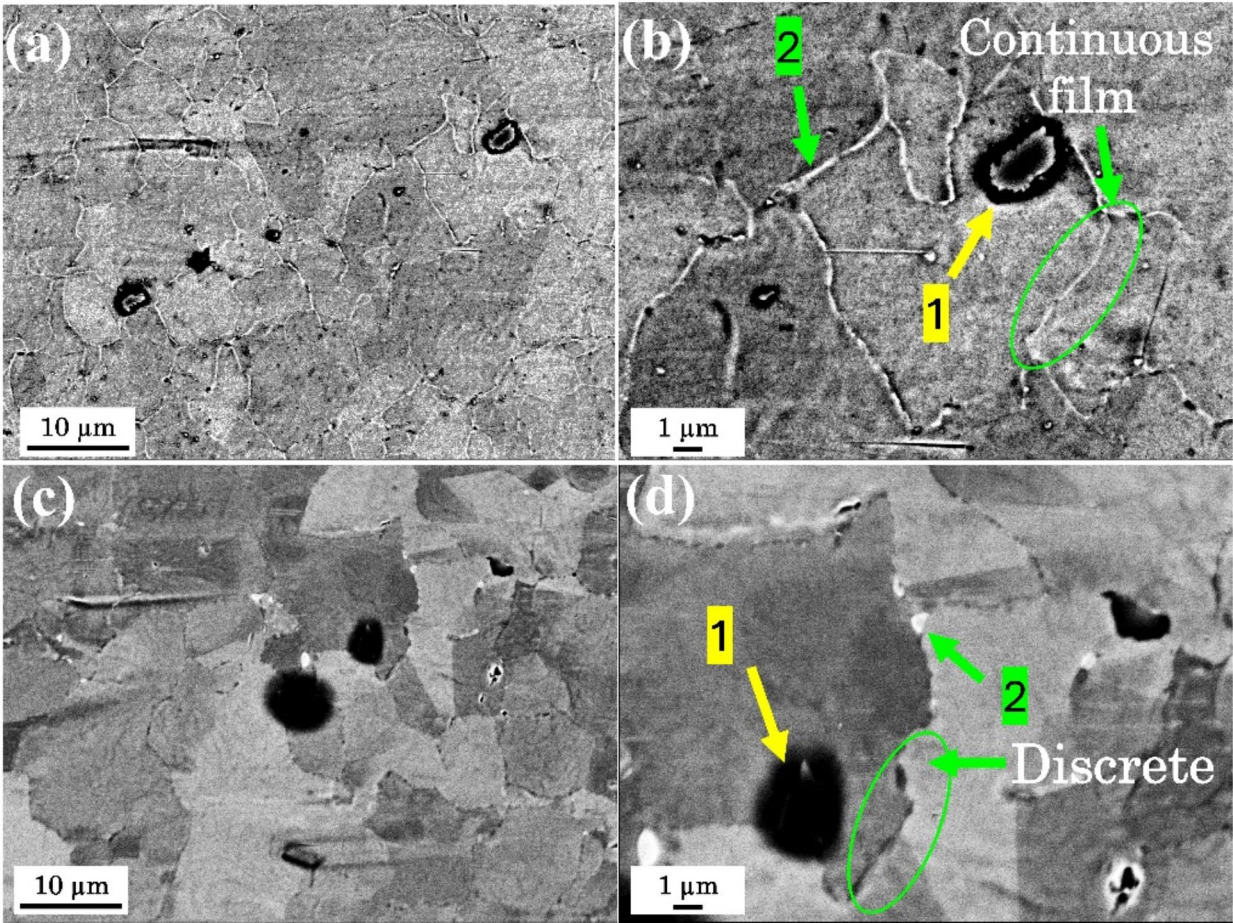
Fig. 6. BS-SEM micrographs of the SZ of the FSWed alloy (a-b) as-welded and (c-d) after aging treatment.

Analysis point	Ni	Mo	Cr	Ti	Al
As-welded					
Ti-Mo rich phase (MC): **1**	6.54	33.22	4.66	53.25	-
Cr-rich phase ($M_{23}C_6$): **2**	63.19	9.15	23.53	2.49	1.61
Aged					
Ti-Mo rich phase (MC): **1**	4.32	35.14	4.03	54.35	-
Cr-rich phase ($M_{23}C_6$): **2**	64.00	8.95	22.86	2.49	1.70

Table 3. EDS elemental composition (at%) of the points shown in Fig. 6.

$M_{23}C_6$ phase owing to the grain boundary motion accompanied by the two-step aging treatment. However, in the present study, grain growth was not observed in the aged specimen owing to the grain boundary pinning effect by these carbide phases during the first stage of aging heat treatment. Therefore, the $M_{23}C_6$ carbide phase is mainly observed at the grain boundaries.

Figure 7 (a-c) and (d-f) display bright field scanning tunneling electron microscope (BF STEM) micrographs of the SZ in the FSWed H282 alloy before and after aging heat treatment, respectively. Before aging, the microstructure of the FSWed alloy primarily features a randomly dispersed MC-type carbide phase (indicated by yellow arrows) both along the grain boundaries and within the grain interior. Notably, Fig. 7(c) reveals the presence of a $M_{23}C_6$ carbide phase, forming a continuous film predominantly along the grain boundaries of the unaged FSWed alloy, as previously discussed. In contrast, the microstructure of the aged specimen (Fig. 7(d-f)) highlights MC, $M_{23}C_6$ (marked by white arrows), and γ′ as the principal constituent phases. The Cr-rich $M_{23}C_6$ carbide phase appears in a discrete "stone-wall" morphology, as evident in Fig. 7(f) and the corresponding elemental mapping in Fig. 7 (f1-f4). The high intensity of Cr (Fig. 7(f2)) confirms that the discrete particles are Cr-rich $M_{23}C_6$ carbide phases. The dark-field TEM micrograph illustrated in the inset of Fig. 7(f) represents the extremely fine γ′ phase that precipitated within the γ matrix following the two-stage aging heat treatment.
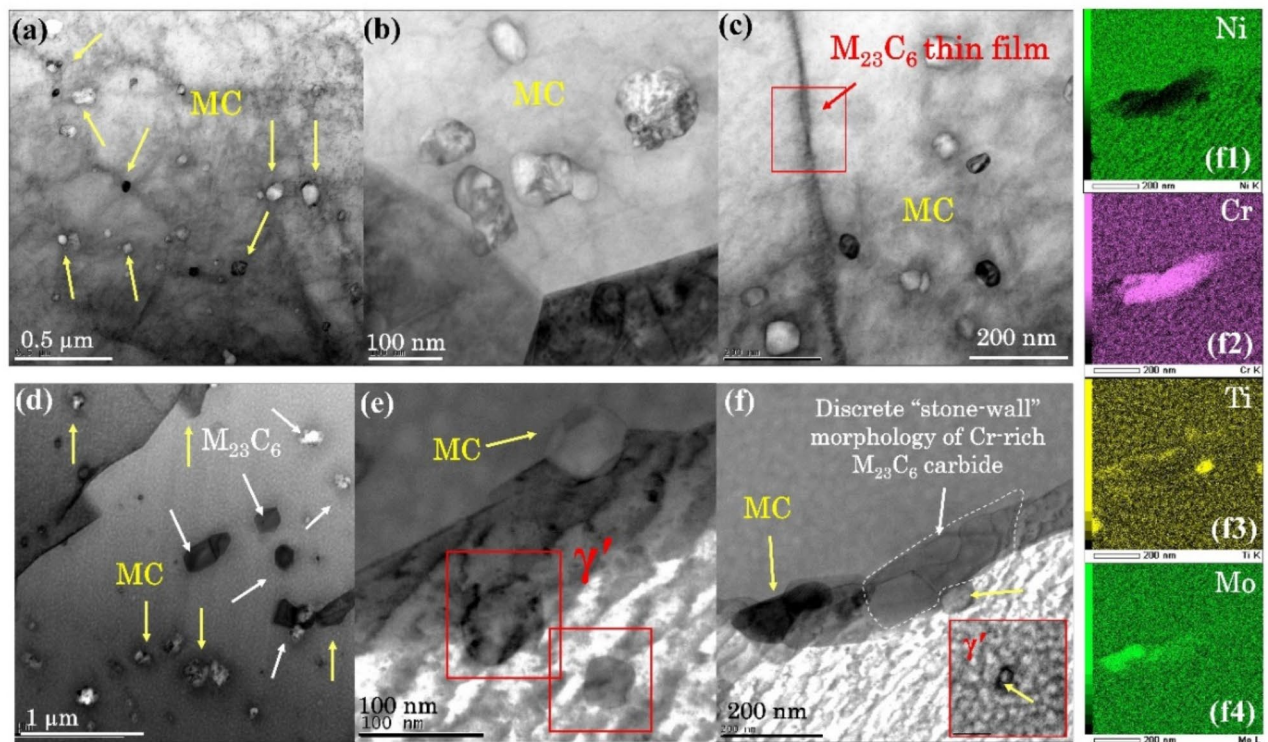
Fig. 7. BF STEM micrographs of the FSWed H282 alloy (a-c) before and (d-f) after aging heat treatment. (f1-f4) EDS elemental mapping of (f). The yellow and white arrows indicate the MC and $M_{23}C_6$ carbide phases, respectively.

Additionally, Fig. 7(e) shows some coarse cuboid-shaped γ' phase precipitates near the grain boundaries. EDS elemental mapping (Fig. 2s, supplementary information) of these particles via TEM reveals a high atomic fraction of Ti and Al, further confirming that these phases are the γ' phase. Additionally, Fig. 8 displays high-magnification BF-STEM micrographs, selected area electron diffraction (SAED) patterns, and dark field TEM images of the γ' precipitate, $M_{23}C_6$, and MC carbide phases in the aged FSW joint specimen. The corresponding EDS elemental composition is shown in Table 4. Together, Fig. 8; Table 4 provide further confirmation of the identities of these phases in the FSWed aged specimen.

Mechanical properties

Figure 9(a) shows the microhardness distribution of the base material and friction stir welded (FSW) joints before and after aging heat treatment. The weld zone of the as-welded joint (FSW specimen) exhibits a considerably higher microhardness than the average microhardness of the as-received base material (indicated by a black dashed line). This increased hardness is largely attributed to the presence of carbides and a fine-grained, recrystallized microstructure resulting from severe plastic deformation during FSW. However, the microhardness distribution also reveals a softened region at approximately 4 mm from the weld center on both AS and RS, corresponding to a narrow heat-affected zone (HAZ). This softened region is also identified as the area of stress concentration during tensile testing, as discussed later in this section. Additionally, after the two-step aging heat treatment, the microhardness of the weld zone increased significantly from approximately 300–350 HV under the as-welded condition to approximately 425–450 HV because of the precipitation of the γ' strengthening phase. Here, the microhardness of the base material increased from approximately 300 HV to 400 HV.

Figure 9(b) presents the nominal tensile stress–strain curves for the base material and FSWed joints before and after aging heat treatment, with the tensile properties summarized in Table 5. The ultimate tensile strength (UTS)-based weld efficiency of the FSW joint before aging was approximately 96.3%, although the ductility was significantly reduced by around 43%. After aging heat treatment, the UTS-based weld efficiency improved to 100%, with only 15% loss in the ductility compared with that of the base material in the aged condition (BM-AG). Notably, both the strength and ductility of the FSWed specimen increased after aging compared to the as-welded condition. The enhanced strength of the FSW joint-AG specimen as compared to the FSW-joint specimen is attributed to the increased hardness resulting from the precipitation of the γ' phase. Meanwhile, the improved ductility is linked to the discrete morphology of $M_{23}C_6$ carbides in the FSW joint-AG specimen, contrasting with the continuous thin film morphology observed in the FSW joint specimen, as previously discussed. Interestingly, the proof stress of the FSW joint specimen is higher than the BM specimen even though the FSW specimen was
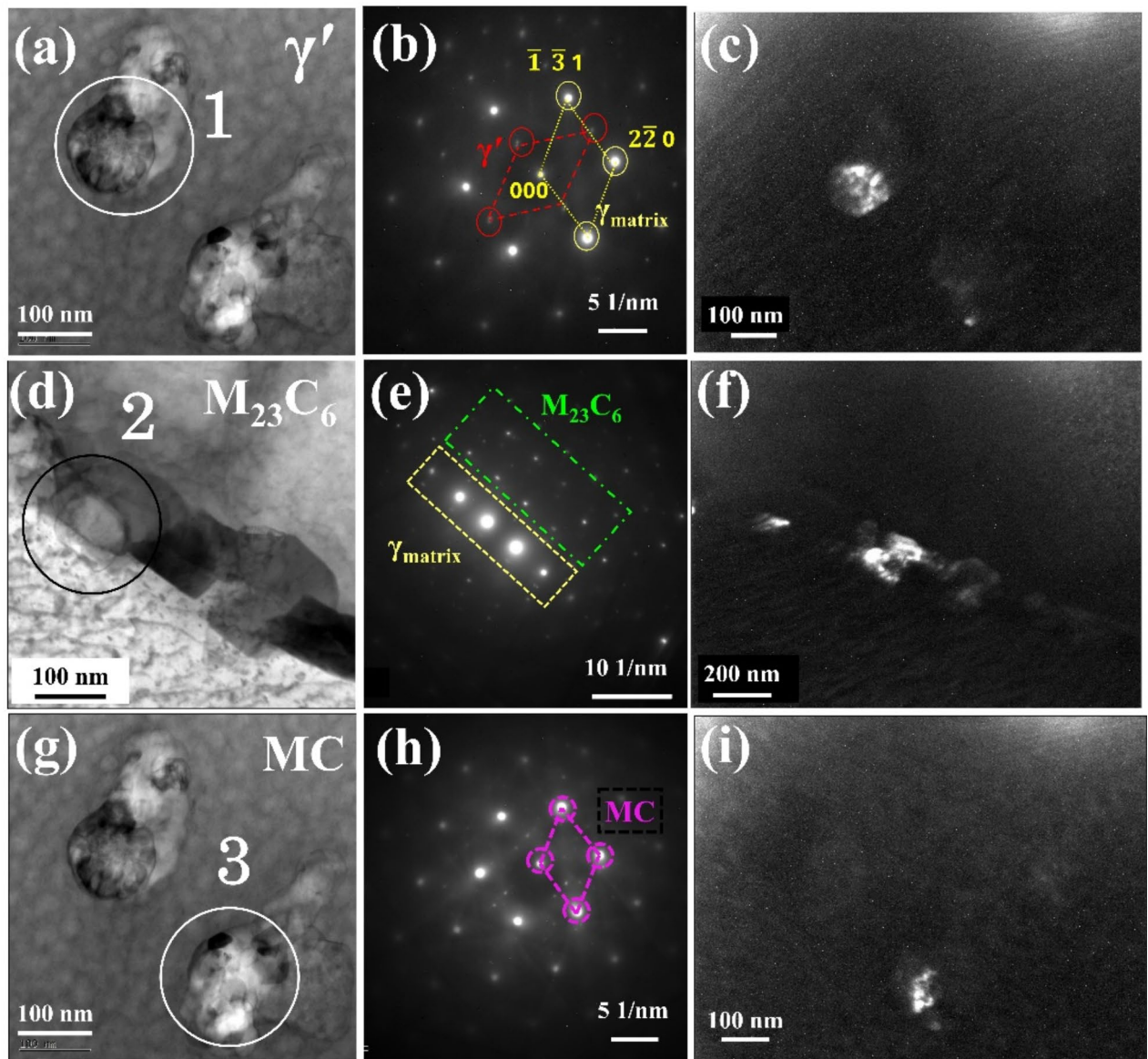
Fig. 8. (a-c) BF-STEM micrograph, SAED pattern and dark field micrograph of (a-c) γ′ precipitate, (d-f) M23C6 carbide, and (g-i) MC carbide, respectively in the aged FSWed specimen.

Analysis point	O	Al	Ti	Cr	Fe	Co	Ni	Mo
$\gamma'-1$	7.02	11.94	4.81	17.28	0.45	8.68	45.3	4.51
$M_{23}C_6-2$	5.08	0.25	20.13	54.89	0.19	1.87	6.80	10.78
$MC-3$	1.91	1.62	31.73	14.47	0.39	6.97	37.09	5.82

Table 4. EDS elemental composition of the particles shown in Fig. 8.

also fractured from the base metal region. This phenomenon is attributed to the large deviation (295 ± 50 HV) in the microhardness of the BM specimen (see Fig. 3s (supplementary information)).

Figure 10 (a-b) and (c-d) illustrate the evolution of localized strain during uniaxial tensile loading of the BM specimen and the FSWed joint specimen after aging heat treatment, respectively. Firstly, the strain evolution in the BM specimen is discussed here. Figure 10 (a) and (b) show that, during elastic loading, the strain is low and uniformly distributed (1). As loading progresses, the specimen begins to yield, marked by an increase in strain in the parallel Sect. (2). During the yield stage, plastic deformation develops further in this Sect. (3). Hardening initiates at (4), leading to an additional increase in strain. By stage (5), the strain distribution becomes uneven at the ultimate tensile strength (UTS), with the specimen fracturing at the point of maximum plastic deformation
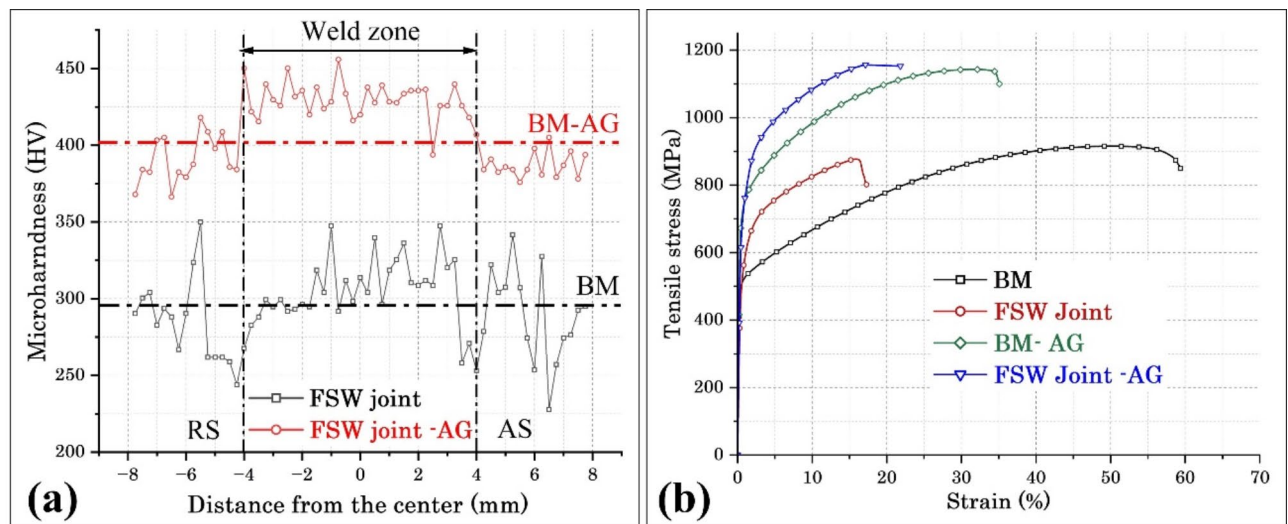
Fig. 9. (a) Microhardness distribution and (b) nominal tensile stress–strain plots of the welded region and base material before and after aging heat treatment. (black and red dotted lines in (a) represents the average hardness values)

	UTS (MPa)	0.2% Proof Stress (MPa)	Elongation (%)
Before Aging			
BM	912±4	503±3	59.5±0.3
FSW Joint	879±10	543±5	16.5±0.9
After aging			
BM -AG	1144±6	737±6	36.3±0.2
FSW joint -AG	1167±0.5	681±11	20.8±1.9

Table 5. Mechanical properties of the BM and FSWed joint before and after aging heat treatment.

(6). The difference in strain between stages 5 and 6 indicates that the BM specimen exhibits higher local elongation than the FSWed specimen, which will be discussed next.

The strain evolution in the FSWed specimen is completely different from that of the BM sample, as evident from Fig. 10 (c) and (d). The strain evolution in the FSWed specimen follows a two-step yielding. The elastic loading (1) is followed by a first yield, which occurs on the base metal region at RS (2). The plastic deformation was developed on both sides of the first yielding region, and its progression was obstructed by the high-strength weld on one side and the flange of the specimen on the other side. However, the onset of the first yield step is also associated with the consequent hardening and plastic deformation. Next, the second yield was initiated on the base metal region at the AS, followed by hardening and increased plastic deformation on both the AS and RS sides (3 and 4). Figure 4s (supplementary information) clearly displays the two yielding phenomena with a 0.05 offset applied to the strain values on the x-axis. The hardening and plastic deformation on the localized AS and RS sides continue to increase until the maximum strength is reached (5), followed by fracture on the AS (6). Interestingly, the absence of visible yield stages in the stress-strain (SS) curve (Fig. 10 (c)) can be attributed to both yielding events occurring at a very localized level without a significant time gap. While strain mapping confirms the presence of these two stages, they do not appear as separate yield points on the SS curve.

The two-step yielding phenomenon in the FSWed specimen is attributed to the high microhardness and strength of the welded region. In the BM specimen, the yielding initiates at the weakest spot in the parallel section of the specimen followed by its rapid propagation to the other regions. In contrast, in the FSWed specimen, the base metal region on either side of the weld has a coarse grain structure as compared to the dynamically recrystallized fine-grained structure of the SZ and deformed grains of the TMAZ region. As a result, the base metal region on either side of the weld has a low yield strength and tensile strength. These regions become preferential sites for stress concentration and localized plastic deformation during tensile loading, as evident from Fig. 10 (d). The weld with high hardness and strength served as an obstruction to prevent the further development of this plastic deformation to the other regions of the specimen and thereby avoid the fracture from the welded region. However, the occurrence of fracture on the AS can correlated with the high temperature and thinning occurred at the AS (see Fig. 2(b) and (d)). At high temperature, although the grain growth may not be that significant, it may have changed the morphology of the carbides at a very local level. These could be
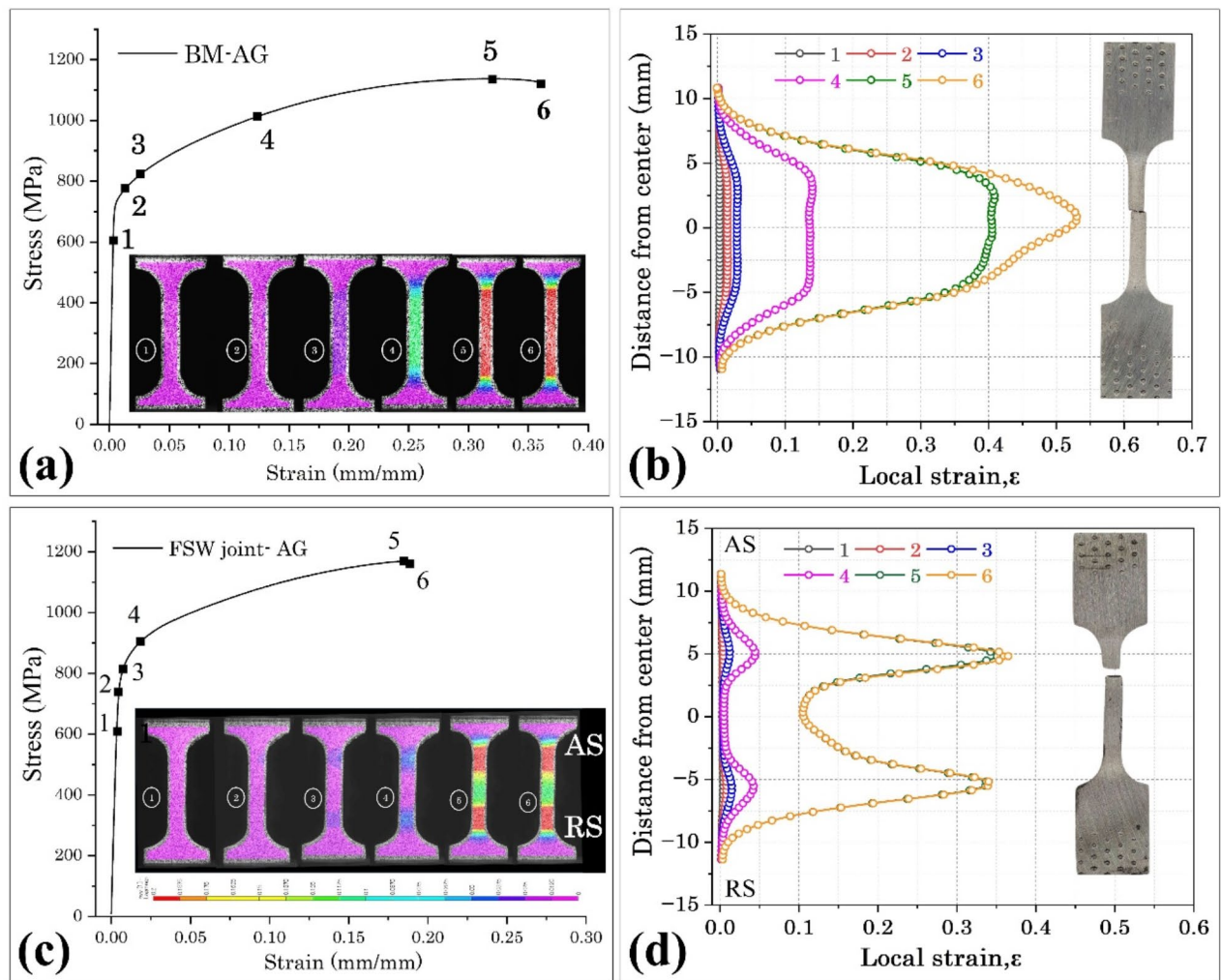
Fig. 10. Nominal tensile SS curve and local strain distribution in the aged (a-b) BM and (c-d) FSWed joint, respectively.

the reasons for the stress concentration on the AS followed by the fracture. However, a detailed fracture study is required to confirm this hypothesis.

Tool condition after FSW

Tool life is a critical factor in the FSW of Haynes 282 alloy. Preliminary results on tool life are presented in Fig. 11. Figure 11 (a-c) depicts the tool surface condition after welding distances of 0, 146, and 238 mm, respectively. Figure 11 (d) shows the tool surface profile, providing a quantitative measurement of tool wear. The results indicate no significant wear phenomena such as adhesion or abrasion on the tool surface. Although these are initial findings, they suggest that the hemispherical tool profile has a favourable impact compared to the conventional tools, where tool probe fractures are common with the Haynes 282 Ni superalloy. Further detailed investigations are needed to predict the actual tool life of the proposed tool for the FSW of high-temperature-strength metallic materials such as the Haynes 282 Ni superalloy.

Conclusion

In the present investigation, friction stir welding (FSW) of a Haynes 282 Ni superalloy was successfully conducted by using a novel hemispherical tool made of Si_3N_4.

A joint efficiency of ~96% was achieved in the as-welded condition, which further increased to 100% following two-step post-weld aging heat treatment. The ductility of the joint increased from 16.5% in the as-welded state to approximately 21% after aging despite the significant increase in strength. This improvement was due to the change in the morphology of the $M_{23}C_6$ carbide phase along the grain boundaries, which shifted from a continuous film to discrete particles after aging. Grain refinement and γ' precipitation hardening are identified as important strengthening mechanisms in the as-welded condition and after aging, respectively. Finally, the preliminary results on tool life reveal no significant tool wear, at least up to a welding distance of ~200 mm.
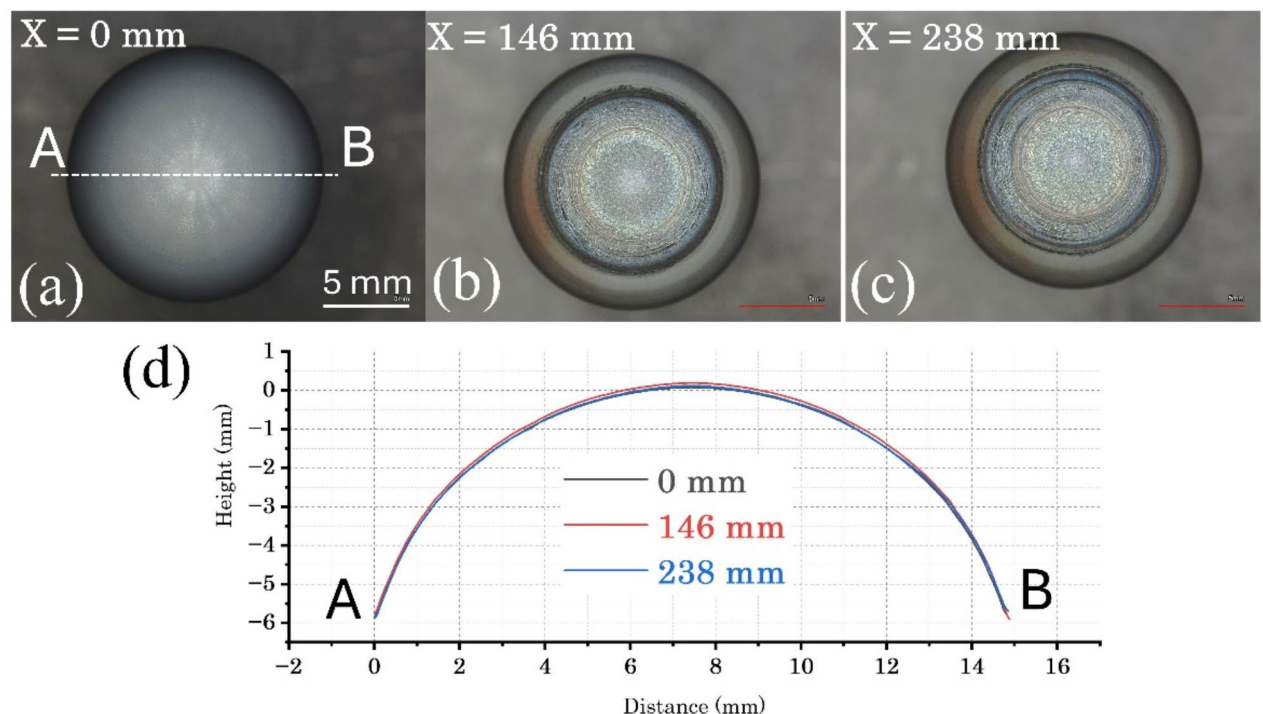
Fig. 11. (a-c) Macrographs and (d) profiles of the tool surface after welding distances (X) of 0, 146 and 238 mm.

Data availability

All data generated or analysed during this study are included in this published article and its supplementary information files.

References

1. Joseph, C., Persson, C. & Hörnqvist Colliander, M. Influence of heat treatment on the microstructure and tensile properties of Ni-base superalloy Haynes 282. *Mater. Sci. Eng. A*. **679**, 520–530 (2017).
2. Yin, H., Gao, Y. & Gu, Y. Effects of post-welding heat treatment on microstructure and mechanical properties of welding joint of new Ni-Fe based superalloy with Haynes 282 filler metal. *Mater. Sci. Eng. A*. **708**, 118–128 (2017).
3. Osoba, L. O., Ding, R. G. & Ojo, O. A. Microstructural analysis of laser weld fusion zone in Haynes 282 superalloy. *Mater. Charact.* **65**, 93–99 (2012).
4. Joseph, C., Persson, C. & Hörnqvist Colliander, M. Precipitation kinetics and morphology of Grain Boundary carbides in Ni-Base Superalloy Haynes 282. *Metall. Mater. Trans. A*. **51**, 6136–6141 (2020).
5. Shaikh, A. S., Schulz, F., Minet-Lallemand, K. & Hryha, E. Microstructure and mechanical properties of Haynes 282 superalloy produced by laser powder bed fusion. *Mater. Today Commun.* **26**, 102038 (2021).
6. Zhang, H., Wang, Y., De Vecchis, R. R. & Xiong, W. Evolution of carbide precipitates in Haynes® 282 superalloy processed by wire arc additive manufacturing. *J. Mater. Process. Technol.* **305**, 117597 (2022).
7. Singh, S., Kadoi, K., Ojo, O., Alexandrov, B. & Andersson, J. The effects of chemistry variations on hot cracking susceptibility of Haynes® 282® for aerospace applications. *Mater. Des.* **228**, 111853 (2023).
8. Singh, S., Andersson, J. & Kadoi, K. Microstructure gradient formation in electron-beam melting powder-bed fusion of a gamma-prime Ni-based superalloy. *Mater. Charact.* **205**, 113370 (2023).
9. Sharma, A., Das, T. & Paul, J. Performance evaluation of Al6061-graphene nanocomposites surface engineered by a novel multiple microchannel reinforcement approach in friction stir processing. *Carbon Lett.* https://doi.org/10.1007/s42823-021-00230-9 (2021).
10. Sharma, A., Morisada, Y. & Fujii, H. Interfacial microstructure and strengthening mechanisms of SPSed Al/GNP nanocomposite subjected to multi-pass friction stir processing. *Mater. Charact.* **197**, 112652 (2023).
11. Ye, F., Fujii, H., Tsumura, T. & Nakata, K. Friction stir welding of Inconel alloy 600. *J. Mater. Sci.* **41**, 5376–5379 (2006).
12. Song, K. H. & Nakata, K. Effect of precipitation on post-heat-treated inconel 625 alloy after friction stir welding. *Mater. Des.* **31**, 2942–2947 (2010).
13. Song, K. H. & Nakata, K. Microstructural and mechanical properties of friction-stir-welded and post-heat-treated Inconel 718 alloy. *J. Alloys Compd.* **505**, 144–150 (2010).
14. Komarasamy, M. et al. Microstructure and mechanical properties of friction stir welded Haynes 282. *Mater. Charact.* **182**, 111558 (2021).
15. Ambrosio, D., Morisada, Y., Ushioda, K. & Fujii, H. Extremely thin intermetallic layer in dissimilar AA6061-T6 and mild steel friction stir lap welding using a hemispherical tool. *Sci. Rep.* **14**, 1718 (2024).

16. Ambrosio, D., Morisada, Y., Ushioda, K. & Fujii, H. Asymmetry in microstructure and mechanical properties of FSWed joints using a hemispherical tool tilted towards the retreating side. *J. Manuf. Process.* **119**, 32–45 (2024).
17. Mori, M., Ban, T., Takeuchi, H., Morisada, Y. & Fujii, H. Friction Stir Welding of Thick Steel Plate Using Silicon Nitride Tool. *ISIJ Int.* **64**, 958–965 (2024).
18. Funaki, K. et al. Elucidation of tool wear phenomenon in FSW using silicon nitride tool. *Weld. Int.* **38**, 500–510 (2024).
19. Ambrosio, D., Sharma, A., Mukuda, M., Morisada, Y. & Fujii, H. Feasibility of friction stir welding using a hemispherical tool tilted towards the retreating side. *J. Adv. Join. Process.* **9**, 100180 (2024).
20. Sharma, A., Morisada, Y. & Fujii, H. Bending induced mechanical exfoliation of graphene interlayers in a through thickness Al-GNP functionally graded composite fabricated via novel single-step FSP approach. *Carbon N Y.* **186**, 475–491 (2022).
21. Osoba, L. O. & Ojo, O. A. Influence of laser welding heat input on HAZ cracking in newly developed Haynes 282 superalloy. *Mater. Sci. Technol.* **28**, 431–436 (2012).
22. Eriksson, E. & Hörnqvist Colliander, M. Dynamic and post-dynamic recrystallization of Haynes 282 below the secondary Carbide Solvus. *Met. (Basel).* **11**, 122 (2021).

Acknowledgements

Author contributions

AS: Data curation, investigation, writing—original draft, fund acquisition. TM: Investigation. YM: Supervision, Writing- review & editing. KU: Investigation, data analysis, Writing−review & editing. SS: Resources. HF: Supervision, Project management, Writing- review & editing.

Declarations

Competing interests

The authors declare no competing interests.

Additional information

Supplementary Information The online version contains supplementary material available at https://doi.org/10.1038/s41598-024-79331-0.

Correspondence and requests for materials should be addressed to A.S. or H.F.

Reprints and permissions information is available at www.nature.com/reprints.

Publisher's note Springer Nature remains neutral with regard to jurisdictional claims in published maps and institutional affiliations.